

# Low-voltage onset of electroluminescence in nanocrystalline-Si/SiO<sub>2</sub> multilayers

A. Anopchenko,<sup>1,a)</sup> A. Marconi,<sup>1</sup> E. Moser,<sup>1</sup> S. Prezioso,<sup>1,b)</sup> M. Wang,<sup>1,c)</sup> L. Pavese,<sup>1</sup> G. Pucker,<sup>2</sup> and P. Bellutti<sup>2</sup>

<sup>1</sup>*Dipartimento di Fisica, Laboratorio di Nanoscienze, Università di Trento, Via Sommarive 14, 38100 Povo (Trento), Italy*

<sup>2</sup>*Microtechnologies Laboratory, Fondazione Bruno Kessler, Via Sommarive 18, 38100 Povo (Trento), Italy*

(Received 14 February 2009; accepted 8 July 2009; published online 11 August 2009)

Thin film metal-oxide-semiconductor light emitting devices (LEDs) based on nanocrystalline silicon multilayer structure were grown by plasma-enhanced chemical vapor deposition. Room temperature electroluminescence was studied under direct current and time-resolved pulsed-current injection schemes. Multilayer LEDs operating at voltages below 5 V and electroluminescence turn-on voltage of 1.4–1.7 V are demonstrated. The turn-on voltage is less than 3.2 V which corresponds to the barrier height at the silicon oxide interface for electrons. Electrical injection in the multilayer LED is controlled by direct tunneling of electrons and holes among silicon nanocrystals. This injection regime is different than the Fowler–Nordheim tunneling that controls the electron injection in single thick layer LED operating at high voltages. A comparison of the power efficiency for the multilayer based LED and a similar single thick layer LED shows larger power efficiency for the former than for the second. Our results open new directions in the development of highly efficient room temperature silicon based LED. © 2009 American Institute of Physics. [DOI: 10.1063/1.3194315]

## I. INTRODUCTION

The improvement in the efficiency of nanocrystalline silicon (nc-Si) light emitting device (LED) has been a topic of intensive research over the past years.<sup>1–3</sup> In spite of many efforts, the reported device efficiencies are still low. There are several reasons for this. A poor quality of the nanocrystalline composite material (formed by nc-Si and SiO<sub>x</sub>) yields parasitic current paths, while the low density of nanocrystals makes direct charge injection into the nanocrystals difficult. Consequently, electroluminescence (EL) is observed only at voltages that are normally much higher than 4.2 V,<sup>3</sup> the value of the barrier at the silicon oxide interface for electrons.<sup>4</sup> At these voltages, Fowler–Nordheim tunneling of hot electrons into the oxide conduction band occurs; EL is then produced by recombination of electron-hole (e-h) pairs in the nc-Si which have been excited by the current of hot electrons via an impact excitation mechanism. The impact excitation mechanism is inefficient while hot electron injection damages the oxide. Thus LEDs based on these mechanisms have both a poor low efficiency and a short lifetime.

In this work, to improve nanocomposite quality and to achieve efficient EL nc-Si based LED, we use a multilayer (ML) structure. It is formed by sequential depositions of a silicon rich oxide layer and a silicon oxide layer. The ML structure allows the control of nanocrystal formation since the constrained growth<sup>5–9</sup> and the design of the effective energy barrier in the current flow direction via the control of the silicon oxide thickness. The constrained nanocrystal

growth is also accompanied by more uniform nanocrystal sizes and a higher nanocrystal areal density than in the usual homogeneous layer deposition. In addition, the quality of the silicon oxide in the barrier layer is higher (fewer defects) than the quality of the oxide matrix resulting from the phase separation.<sup>10</sup> For these reasons, ML nc-Si/SiO<sub>2</sub> structures have been studied both in the past<sup>7,11–13</sup> as well as more recently.<sup>8,14–16</sup> In this work, we will show that ML nc-Si LEDs have superior properties with respect to a single layer nc-Si LED. These include low turn-on voltages, low leakage currents, and high power efficiency.

## II. EXPERIMENTAL

The device structure is a metal-oxide-semiconductor (MOS) capacitor. Alternating layers of stoichiometric SiO<sub>2</sub> and silicon rich silicon oxide (SRO) with a large Si excess were grown by plasma-enhanced chemical vapor deposition (PECVD). These are used as the gate oxide in the MOS. The SRO layer within the ML structure has the following composition: 52 at. % of silicon, 44 at. % of oxygen, and 4 at. % of nitrogen, which has been measured by x-ray photoelectron spectroscopy. The pair of SiO<sub>2</sub> and SRO layers forms the ML period. In this work we detail, in particular, two devices, W9 and W10: the thicknesses of the SRO layer within the ML period were 3 nm for the W9 device and 4 nm for the W10 device. The thickness of the oxide layer was 2 nm in both devices. This layer thickness is a nominal value based on a previous careful characterization of the deposition rates. The number of ML periods is 5. The gate is formed by 100 nm thick *n*-type *in situ* doped polycrystalline silicon (poly-Si), while 500 nm thick Al (1% Si) is used to connect the gate area of  $7.94 \times 10^{-8}$  m<sup>2</sup> with the bonding pad. The poly-Si is covered by an antireflective coating formed by a 50 nm thick

<sup>a)</sup>Electronic mail: anopchenko@science.unitn.it.

<sup>b)</sup>Present address: Department of Physics, University of L'Aquila, Via Vetoio, 67010 Coppito (AQ), Italy.

<sup>c)</sup>Permanent address: State Key Laboratory of Silicon Materials, Zhejiang University, Hangzhou 310027, People's Republic of China.

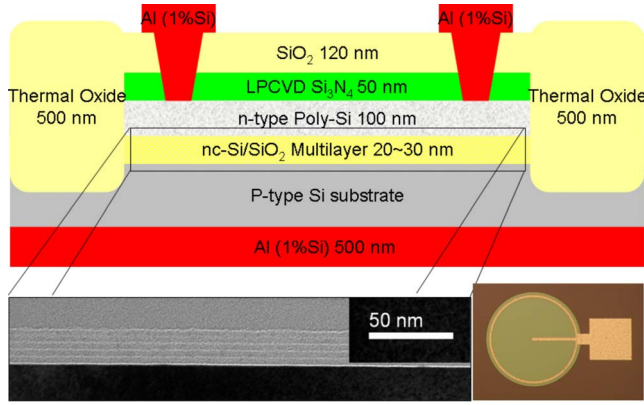


FIG. 1. (Color online) LED schematic cross section (top), top view of the LED (bottom right), and TEM image (bottom left) of the nc-Si/SiO<sub>2</sub> ML (annealed structure of SRO 4 nm/SiO<sub>2</sub> 2 nm, five periods).

Si<sub>3</sub>N<sub>4</sub> layer and a 120 nm thick SiO<sub>2</sub> layer to improve light extraction. Wet oxidation was performed at 1150 °C for 30 min to grow both a 480 nm thick field oxide (for active area isolation) and the Si nanocrystals in the gate dielectric. The total thickness of the ML was 27 nm (32 nm, depending on the thickness of the SRO), which was controlled by both profilometry and variable angle spectroscopic ellipsometry. The substrate was *p*-type (100) Si with 12–18 Ω cm resistivity. The device layout is shown in Fig. 1 along with a cross-sectional transmission electron microscopy (TEM) image of the W10 device (2 nm SiO<sub>2</sub>/4 nm SRO) ML. The periodic structure is revealed by the alternating white and gray stripes, where the white stripes are the SiO<sub>2</sub> layers and the gray stripes are the SRO layers.

A series of monitor wafers was prepared, which followed the process flow of the devices except for the definition of the device areas and contacts by photolithography and metallization. These monitor wafers were used for evaluation of layer thickness, photoluminescence (PL), and structural analysis. The actual thickness of the layers is reported in Table I (for details see Ref. 16). The refractive index at 633 nm of the SiO<sub>2</sub> layers is about 1.48, which indicates good stoichiometry of the oxide.

The current-voltage (*I-V*) characteristics were recorded with a HP 4145A semiconductor parameter analyzer. The delay time in the *I-V* measurements was 1 s to balance measurement speed and measurement integrity. The scanning voltage step was 100 mV. The EL signal was collected with a single photon-counting module SPCM-AQR. The total light emission intensity (counts/s) was integrated over the whole visible spectrum. A function generator, Tektronix AFG 3252, was used to drive the device under alternating current

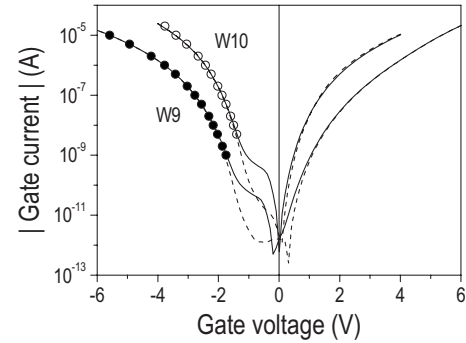


FIG. 2. Current-voltage (*I-V*) characteristics of the ML LEDs. Negative gate voltages correspond to forward bias and positive voltages to reverse bias. Solid lines: scanning the gate voltage from negative-to-positive value. Dashed lines: scanning in the opposite direction, from negative-to-positive voltages. The dots indicate the gate voltages (currents) at which EL signal was recorded. Very weak EL emission was observed under a high reverse bias and no emission at the hysteresis loop.

(ac) or pulsed-current injection scheme. Time-resolved EL signal was recorded with a multichannel scaler SR 430. In the PL experiment, silicon nanocrystals were excited with the 514.5 nm argon laser line at an incident power density of  $\sim 0.5$  W/cm<sup>2</sup>. The EL and PL spectra were collected with a fiber bunch and analyzed by a Spectra-Pro 2300i monochromator coupled with a nitrogen cooled charge coupled device (CCD) camera. The measurements were performed at room temperature in a dark room.

### III. RESULTS AND DISCUSSION

#### A. Optoelectrical characteristics under direct current

The *I-V* characteristics of the W9 and W10 devices are shown in Fig. 2. The logarithm of the absolute value of electrical current is plotted as a function of the applied gate voltage. A negative gate voltage corresponds to forward bias, i.e., the MOS is in accumulation. A positive gate voltage corresponds to reverse bias, i.e., the silicon substrate is in inversion. The *I-V* curves were collected by scanning the device from accumulation to inversion and then backward from inversion to accumulation. An *I-V* hysteresis loop was found in both the W9 and W10 devices, which extends to about 1.4 V under forward bias for the W10 device (1.7 V in the case of W9). This hysteresis is due to charge accumulation or trapping in the device.<sup>17</sup> At these very low voltages, the current might be due to the (inelastic) tunneling into the nc-Si/SiO<sub>2</sub> interface states.<sup>4</sup> The presence of subbandgap interface states has been reported recently by us.<sup>18</sup> The *I-V* characteristics are symmetrical with respect to zero bias; the current is the same under forward and reverse biases, which

TABLE I. Layer thicknesses of the as-deposited SRO/SiO<sub>2</sub> ML structures obtained from ellipsometry; the total thickness of the structures is calculated from the layer thickness and the number of the layers (five layers of SRO and six layers of SiO<sub>2</sub>).

Sample name	Nominal ML thickness	SiO <sub>2</sub> layer thickness (nm)	SRO layer thickness (nm)	Total thickness (nm)
W10	2 nm SiO <sub>2</sub> /4 nm SRO	1.52 ± 0.03	3.12 ± 0.02	24.7 ± 0.3
W9	2 nm SiO <sub>2</sub> /3 nm SRO	1.84 ± 0.03	1.94 ± 0.02	20.7 ± 0.3

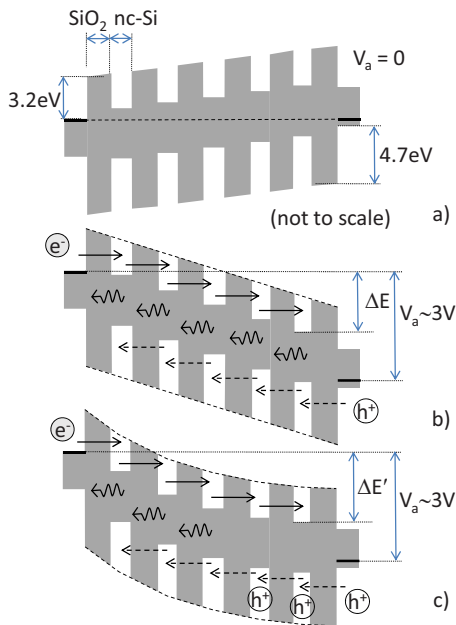


FIG. 3. (Color online) Schematic band diagram of an ideal ML structure (without localized states in the oxide barriers, shorts, etc.) under (a) no bias, (b) low forward bias,  $\sim 3$  V without trapped charges in the oxide, and (c) low forward bias with positive charge trapped near the positively biased electrode.

might indicate a bulk-limited nature of the measured current controlled by the direct tunneling of electrical charges between the nc-Si conduction/valence bands.<sup>19,20</sup> The symmetrical  $I$ - $V$  characteristics from nc-Si MOS-LEDs have been reported in both experimental and theoretical works, see, for example, Refs. 19–22. The  $I$ - $V$  symmetry is related to the symmetry of the energy barrier thicknesses of the oxide containing the nc-Si. The current through the oxide is controlled by the direct charge tunneling among the nanocrystals in the *bulk* of the oxide and, hence, there is a small difference between the current for positive and negative gate voltages. Conduction band electron injection and electron current dominate over hole injection due to the energy barrier height asymmetry. This electron current is symmetric with respect to the gate polarity.<sup>21</sup>

Figure 3 shows a schematic energy band diagram of an ideal ML structure, i.e., without shorts or localized energy states in the silicon oxide matrix, along a conduction path. Gray areas represent the energy gaps in silicon electrodes, nc-Si, and silicon oxide layers. Figure 3(a) shows the band diagram with no bias applied, while Figs. 3(b) and 3(c) show the band diagram under low,  $\sim 3$  V, negative voltage applied to the gate. Figure 3(c) shows the effect of positive charge trapping near the positively biased electrode on the band bending. The straight arrows (solid and dashed) indicate direct charge (electrons and holes) tunneling in the ML structure, i.e., tunneling through the trapezoidal barrier. The wavy arrows stand for light emission from the nc-Si. The excess energy,  $\Delta E$ , that electrons can gain by tunneling (elastically) through the oxide (five silicon oxide layers) increases to  $\Delta E'$  when some positive space charge is built up (trapped) on the Si nanocrystals near the positively biased electrode, compare Figs. 3(b) and 3(c).

It has to be noticed that even at low voltages (electric fields), injection current into the silicon nanocrystals could be large provided that the tunneling oxide thickness is small, normally smaller than 2 nm.<sup>4,23,24</sup> For example, single electron injection current into a spherical nanocrystal having a diameter of 5 nm with a 1.5 nm tunneling oxide could be a few femtoamperes at the applied voltage of about 3 V.<sup>25</sup> Multiplying this value by a typical density of the nc-Si in the ML structure, which is of the order of  $10^{12}$  cm<sup>-2</sup>, and by the area of our device, the injection current amounts to a few microamperes, which well compares with the measured tunneling currents in Fig. 2.

The W10 device with thicker SRO layers has a higher conductivity than the W9 device with thinner SRO layers. The average silicon content in the W10 is 45 at. %, while it is 44 at. % for the W9 device.<sup>16</sup> Taking this into account, a higher conductivity in W10 could be expected because of its higher silicon excess.<sup>17,22</sup> However, for a ML structure it is the silicon oxide thickness that determines the device conductivity in the tunneling processes. Although both devices have the same nominal thickness of the oxide, the actual values obtained from ellipsometry studies are different, namely: 1.5 nm for W10 and 1.8 nm for W9 (see Table I).<sup>16</sup> We believe that this is the main source of the difference in the device conductivities.

The current (voltage) values at which EL emission in the visible–near-infrared region was recorded are marked with open and closed dots in Fig. 2. Strong emission is observed for forward bias [Fig. 3(c)]. It is important to note that EL emission occurs at low voltages, lower than 3.2 or 4.7 V which are the values corresponding to the height of the energy barriers at the silicon oxide interface for electrons or holes, respectively [Fig. 3(a)]. The light emission at these low voltages is due to the bipolar (electrons and holes) injection into the nc-Si via the direct tunneling mechanism.<sup>26</sup> Very recently the bipolar character of charge injection in the nc-Si ML under low applied voltages was experimentally confirmed by our group.<sup>27</sup> At this low bias values, the EL emission is not due to the hot carrier injection and impact ionization of the nanocrystals.

The onsets of EL voltages are as low as 1.4 and 1.7 V for the W10 and W9 devices, respectively. These are the lowest turn-on voltage values reported so far for this type of devices.<sup>3</sup> In a simple interpretation, these values correspond to the fundamental optical energy gaps of the involved nc-Si. The corresponding diameters of the spherical silicon nanocrystals with the optical gaps of 1.7 and 1.4 eV are 1.92 and 3.21 nm, respectively.<sup>28</sup> These values are a result of the quantum-confinement effects calculated within the density functional theory (DFT) by Seino *et al.*<sup>28</sup> Although the energy gap value of bulk silicon is underestimated by the DFT, the confinement energies, i.e., the difference between excitation energies and the bulk gap, seem to be overestimated with respect to experimental values reported by Heitmann *et al.*<sup>29</sup> These nanocrystal diameters are in good agreement with the SRO thickness values obtained from ellipsometry for the W9 and W10 devices, respectively (Table I).

When high biases ( $>3.2$  or 4.7 V) are applied, the field-enhanced Fowler–Nordheim tunneling into oxide

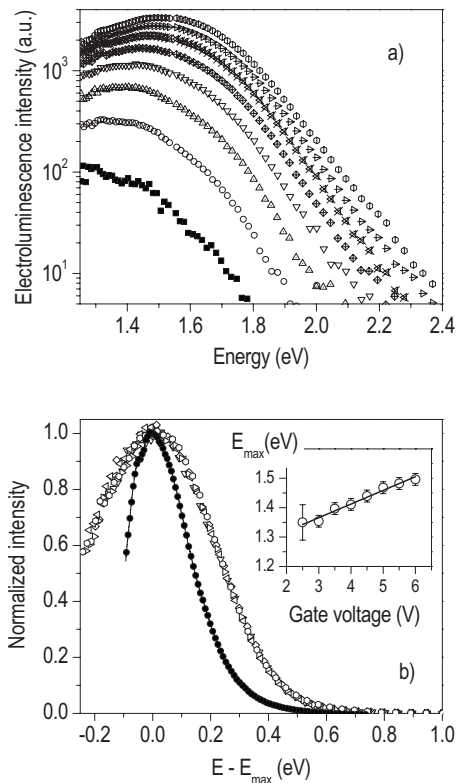


FIG. 4. (a) EL spectra of wafer W9 (2 nm SiO<sub>2</sub>/3 nm SRO) at different gate voltages; from the bottom up: 2.5, 3, 3.5, 4, 4.5, 5, 5.5, and 6 V. (b) The same EL spectra normalized to the peak intensity and shifted along the *x*-axis according to the peak energy value. The peak energy as a function of applied gate voltage is shown in the inset. Solid symbols are PL data taken from the monitor wafer with 514.5 nm argon laser line at the incident power of 0.5 W/cm<sup>2</sup>. The PL peaks at the energy (wavelength) of 1.37 eV (895 nm).

conduction/valence bands occurs. At the high bias injected charges could also gain sufficient energy to excite the nanocrystals by impact ionization. However, very weak EL emission was observed at high voltages when the gate was positively biased. At this bias polarity the silicon substrate is in inversion and the electrical current is due to conduction band electrons. This indicates that impact ionization does not contribute largely into observed EL emission which is due to the radiative recombination of excitons formed by both electron and hole injection into silicon nanocrystals. The absence of EL emission under reverse bias is due to the fact that the hole tunneling current is negligible at positive gate voltages and conduction band electron current is dominant over the entire voltage range.<sup>21</sup> The heavily doped *n*-type poly-Si gate is not a good source for hole injection into the nc-Si layers when reverse biased. So these observations indicate that direct tunneling into the nc-Si is the predominant mechanism of excitation of EL in our devices.

It is also noteworthy that the light emission is observed at voltages beyond the *I*-*V* hysteresis region. Very weak EL signal (within the sensitivity of our photon-counting module) was observed in the very low forward bias range from 0 to about 1.4 V (W10 device). This suggests that charge trapping (the *I*-*V* hysteresis) is not consistent with EL emission. This has been also pointed in Ref. 30.

EL spectra are shown in Fig. 4. Figure 4(a) shows the EL

spectrum dependence on the applied voltage. Wide EL spectra in the visible–near-infrared region, 500–1000 nm, are observed. The large bandwidth of the emission is a consequence of an inhomogeneous broadening due to the size dispersion of nc-Si. When the applied voltage increases the peak of the EL spectrum shifts toward high energies. A similar shift in the EL peak to higher energies was observed in Ref. 15 but at the temperature of 80 K. This shift is large, almost 150 meV, or 100 nm, for a voltage change of 4 V. This is shown in the inset of Fig. 4(b). The peak energy fits well to a linear function of the applied gate voltage, which is shown in the inset. The extrapolation to 0 V gives a value of  $1.22 \pm 0.02$  eV, which is larger than the bulk silicon indirect bandgap value. Even though this extrapolated value is purely indicative, direct tunneling means that the e-h pair has to be in resonant with the nc-Si states. Hence, at zero bias we are injecting e-h pair into the lowest available state, which corresponds to the largest nc-Si size.

It is well known that the ground state energy of single isolated quantum dots shifts toward lower energy in the presence of a low electric field (in the second order approximation) and the shift is a quadratic function of the field strength.<sup>31</sup> This is also known as the quantum-confined Stark effect. The redshift (to longer wavelengths) of PL emission in the presence of electric field was shown for Si nanocrystals embedded in SiO<sub>2</sub> matrix.<sup>32,33</sup> This effect cannot explain our observations since we observed a blueshift and not a redshift. The strong blueshift of our EL peak wavelength with increasing applied voltages is due to selective injection into the ensemble of size dispersed Si nanocrystals. Larger voltages allow direct charge tunneling into smaller nc-Si and, consequently, the emission shifts to high energies.

To allow a more clear comparison among the EL line-shapes at different biases, the EL spectra were normalized to the peak intensity and plotted in a linear scale in Fig. 4(b). In addition, the spectra were also energy shifted to the peak energy value shown in the inset. The EL spectra superimpose into a single spectrum, showing the same (within the error) EL spectrum full width at half maximum of around 500 meV. The same spectral width (the spectra become a little narrower in the wavelength scale) is in opposite to results on a similar but single layer nc-Si LED, which operates at very high voltages.<sup>22</sup> The authors showed a broadening of the EL spectra under high voltages due to impact excitation of the nc-Si by injected electrons.

The PL spectrum collected from the monitor wafer is also shown in Fig. 4(b). The agreement between both EL and PL spectra is fairly good which points to the same mechanism of radiative recombination. It should be noticed, though, that EL and PL peak energies are the same at a certain applied voltage only, around 3 V. This value is close to the corresponding PL excitation energy of 2.4 eV. The PL spectrum is also narrower than the EL one, which might be due to the averaging over the nc-Si sizes of the photoexcited carriers.

The total EL intensity measured with the photon-counting module as a function of the injected current *I* and applied gate voltage is shown in Fig. 5. For a comparison, the results of similar measurements on a thick single layer

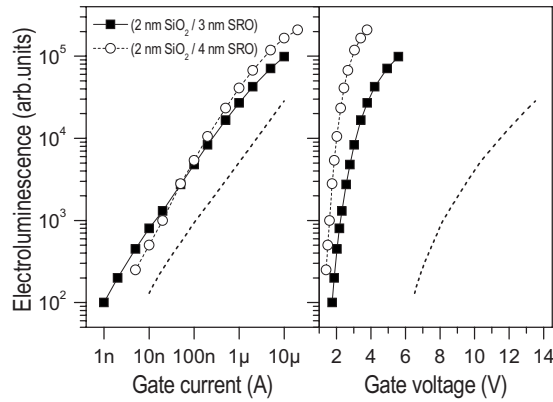


FIG. 5. Total EL intensity as a function of injected current and gate voltage. The dot line is the corresponding EL emission from a single layer LED  $\sim 50$  nm thick having the same average silicon content as the W9 LED, 2 nm  $\text{SiO}_2/3$  nm SRO.

LED are shown. The single thick layer device has the same average silicon content as the ML structure W9 and a thickness of  $\sim 50$  nm. From Fig. 5 it is clear that the ML LED has much better performances than the single layer LED. The operating voltages are largely decreased and are below 5 V while the EL emission is not just kept at the same level but also increased by a factor of 5 (at the same injection current). The overall increase in the LED power efficiency is by a factor of 25. These observations show the relevance of a tight control on the nc-Si dispersions and of the tunneling barriers to optimize the nc-Si injection and yield high EL efficiency. At high injection currents (high voltages) the ML LED efficiency decreases. This may be due to an increase in Fowler–Nordheim tunneling and Auger nonradiative recombination. The Fowler–Nordheim tunneling leads to the generation of nonradiative defects in the SRO layer which in turn decreases efficiency. The W10 device has a larger  $\text{EL}(I)$  slope than the W9 device ( $0.97 \pm 0.02$  versus  $0.8 \pm 0.01$ ). This indicates once more the relevance of controlling the barrier oxide thickness to improve the performance of the LED.

The LED power efficiency is about 0.01% at the injection current of 1  $\mu\text{A}$  (corresponding to a driving voltage of 2.3 V). It was measured with a large area  $p$ - $i$ - $n$  photodiode (UDT PIN-10DF), whose output current signal was measured by a Keithley 6485 picoamperometer. The photodiode was placed within a few millimeters above the device. A simple correction for the collection solid angle was taken into account. The emitted optical power density was about 0.2  $\mu\text{W}/\text{cm}^2$ . The emitted power increases when injection current increases, but the efficiency decreases. Despite this power efficiency value being among the highest reported for this system,<sup>3,27</sup> it is still too low for practical purposes. The low value of the power efficiency might be explained by the fact that the control over the layer thickness in the PECVD machine is still not optimized, since the used machine is a standard commercial one. A precise control of the thickness and composition of such thin layers is a must in order to avoid high field effects which can open parasitic shunting paths or destroy the thin  $\text{SiO}_2$  layers.

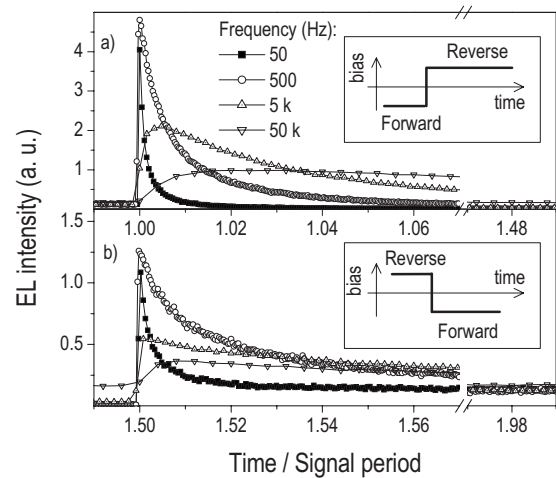


FIG. 6. Time-resolved EL signal in the W9 device, 2 nm  $\text{SiO}_2/3$  nm SRO. The driving gate signal is a square waveform with the rms voltage value of 4 V. (a) EL emission decay at the bias transition from forward to reverse, which is sketched in the inset; (b) EL decay at the bias transition from reverse to forward. The driving gate frequency value is shown in the figure legend.

## B. Time-resolved and pulsed-current electroluminescence

When the direct current (dc) voltage is swept abruptly from positive-to-negative value and vice versa the EL of the nc-Si MOS-LED shows a peak. This was predicted theoretically in Ref. 34 and demonstrated experimentally in Ref. 35. In the former work, bipolar charge injection into nc-Si is studied by Monte Carlo simulations. A perturbation of the static electric field was induced by a larger electric field. This perturbation increases the e-h density in the nc-Si and gives rise to an enhanced EL emission. Alternatively a field-effect EL model was developed in Ref. 35 based on an alternate polarity charge injection from the silicon substrate into the nc-Si which was followed by exciton formation and recombination in the nanocrystals. Both electrons and holes are injected from the silicon substrate into the nc-Si through Fowler–Nordheim tunneling. The injection is not simultaneous and charge leakage brings about an asymmetry in the EL peak intensities at different bias transitions.

We explored these proposed effects by applying a square waveform signal to the gate of our LED. Figure 6 shows the peak EL emission at both negative-to-positive and positive-to-negative bias transitions for the W9 device. It also shows the EL peak decay during the period of constant bias with a root-mean-square (rms) value of 4 V. Figure 6(a) shows EL peak and decay after forward-to-reverse bias transition while Fig. 6(b) shows the EL peak and decay after reverse-to-forward bias transition. The time axis is given in unitless values,  $t/T$ , where  $T$  is the period of the driving square-form voltage signal. The following reasoning might explain the peak EL emission at the bias transitions. Under a constant bias, the holes accumulate at the anode side of the oxide layer containing the nc-Si and the electrons at the cathode side.<sup>34,36</sup> At the bias transitions these charge populations will exchange positions moving toward each other and bringing the peak of EL emission.

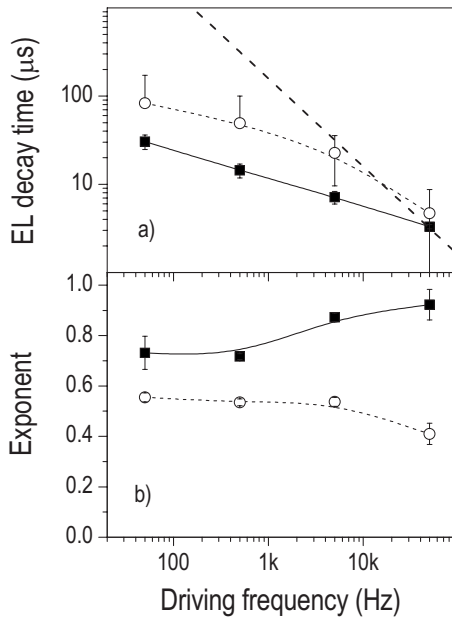


FIG. 7. Parameters of the time-resolved EL signals (Fig. 6) obtained from a fit against the stretched exponential function. Solid symbols correspond to the bias transition from forward to reverse [Fig. 6(a)]; open symbols correspond to the bias transition from reverse to forward [Fig. 6(b)].

The amplitude of the EL peaks is about four times larger for the forward-to-reverse bias transition than for the reverse-to-forward one. This asymmetry might be explained by the difference in electron and hole injection efficiencies from the *n*-type polysilicon gate and *p*-type Si substrate.<sup>35,37</sup> Under forward bias, holes accumulate in the gate oxide in a greater amount than under reverse bias, because hole injection takes place from the accumulation layer in Si substrate. There is a constant EL signal under the forward bias to which the EL peak emission decays after reverse-to-forward bias transition. This constant EL signal under the forward bias is the direct current EL emission.

Figure 6 shows the EL peak decay for several driving frequencies. The peak EL emission decreases when the driving frequency increases for both transitions. This is due to the decrease in the time available for storing charges in the nc-Si layers with increasing frequency.<sup>37</sup> The EL decay could be fitted by a stretched exponential decay equation:

$$I(t) = I(0)\exp[-(t/\langle\tau\rangle)^\beta],$$

where  $\langle t \rangle$  is an effective recombination lifetime (we name it EL decay time) and the exponent  $\beta$  accounts for deviation from the single exponential decay curves ( $\beta=1$ ). The stretched exponential decay is related to the energy transfer relaxation processes among nanocrystals with different dimensions in a dense ensemble. Figure 7 shows the EL decay parameters as a function of the driving frequency for the same device in Fig. 6. Figure 7(a) shows the dependence of the EL decay time for both bias transitions. The EL decay time is larger for the reverse-to-forward bias transitions than for the forward-to-reverse transitions and both decay times decrease when frequency increases. This is because when the driving frequency increases, the injected electrical power increases too. The decrease in EL decay time of Si *p-i-n* diode

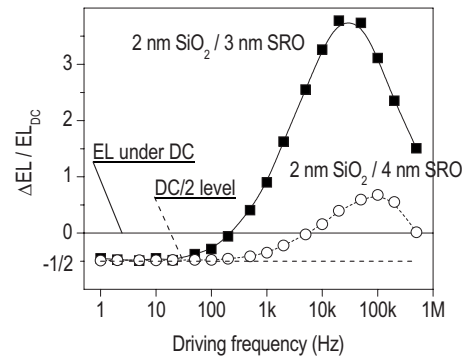


FIG. 8. The increase in total EL emission under ac injection over the EL emission under dc (at the forward voltage of 4 V). The total EL intensity was collected with a CCD camera for the period of 30 s. The ac driving signal is a square waveform with the rms voltage value of 4 V. Solid symbols: W9 device, 2 nm SiO<sub>2</sub>/3 nm SRO; open symbols: W10 device, 2 nm SiO<sub>2</sub>/4 nm SRO.

after application of a reverse bias potential was observed in Refs. 38 and 39 and attributed to the change in the width of the space-charge region.<sup>39</sup> Although no dependence on the current pulse amplitude was observed in these works, a small decrease in the EL decay time with increasing the density of the extra peak current under a pulsed excitation was reported in Ref. 40. Figure 7(b) shows the frequency dependence of the stretched exponent. The difference in the exponent values and the effective decay time corresponding to the two bias transitions might be attributed to the difference in the mobility of electrons and holes that migrate among the nanocrystals in ML ensemble. Electrons have larger mobility than holes and, hence, shorter times and larger exponent value.

The total integrated EL emission as a function of the driving gate frequency is shown in Fig. 8. Figure 8 shows the EL signal integrated over a 30 s period by a CCD camera. At low frequency, the EL emission is the same as under dc bias. When the driving frequency increases, the number of bias transitions in 30 s increases too. Although the peak EL emission at the bias transition decreases when the frequency increases, the EL signal collected in the 30 s period will increase. It peaks at a value of 50 kHz because the mean radiative lifetime becomes equal to the driving gate frequency [the dashed line in Fig. 7(a)]. The EL emission under such a pulsed excitation scheme is larger than for dc by a factor of 4 at the peak (optimal) gate driving frequency. A stronger emission is present up to a gate modulation frequency of 1 MHz. A full modulation of the EL signal exists until the frequency reaches its optimal value of 50 kHz (Fig. 6). The full modulation means that EL emission peaks at the bias transition, decays exponentially, and reaches a steady-state value at longer times. At higher frequency the EL modulation is partial, i.e., the steady-state value is not reached.

Estimation of the power efficiency under pulsed voltage excitation is a difficult task. It requires knowledge of the load impedance, which could not be measured under the pulsed excitation waveform we used. Besides, the measurement is impeded by parasitic capacitances and resistances of the electrical circuit. Charging currents show very sharp and intense peaks at the bias transitions which decay at the nano-

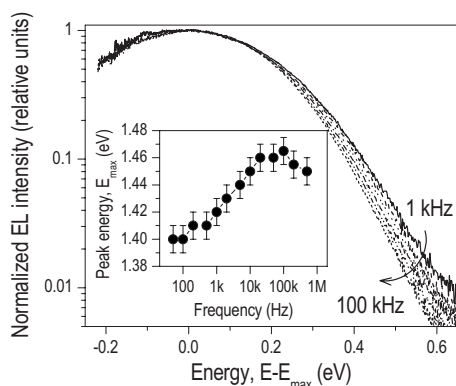


FIG. 9. Normalized EL spectra collected at different ac driving voltage frequencies for the W9 device, 2 nm SiO<sub>2</sub>/3 nm SRO. The frequencies are (from the top to the bottom, in kHz): 1, 2, 5, 10, 20, and 100. The driving gate signal is a square waveform with the rms voltage value of 4 V. The inset shows the EL spectrum peak energy as a function of driving frequency.

second timescale.<sup>40</sup> The field-effect EL power efficiency of similar devices was estimated in Ref. 41 based on the electrical power provided by the voltage source. The value is 0.1%–1%.<sup>41</sup> Our estimate of the power efficiency shows that power efficiency decreases with the driving frequency and it is about four times smaller at 50 kHz than the value at dc. Our estimate is based on the frequency dependence of measured rms value of ac current through the device.

EL spectra collected at different frequencies are shown in Fig. 9. The spectra are normalized in the same manner as the spectra shown in Fig. 4(b): to the peak intensity and peak energy. The peak energy dependence on the driving frequency is shown in the inset. This dependence is consistent with the dependence of the total EL emission shown in Fig. 8. The EL peak energy shifts to higher energies and has a maximum at about 50 kHz, the optimal frequency of EL emission. This blueshift is connected to the decrease in the EL decay lifetime shown in Fig. 7(a). As it was shown in Ref. 37, EL emission at shorter wavelengths peaks at larger driving frequencies than emission at longer wavelengths. Therefore, charge injection into small nanocrystals (more efficient) occurs faster than injection into large nanocrystals.<sup>37</sup> When the gate modulation frequency increases, the EL peak wavelength blueshifts and the effective EL decay time decreases. Variation in the optimal driving frequency at different emission wavelengths was studied in Ref. 37 and used later on to build a white light LED.<sup>42</sup>

Very recently an alternative explanation for the field-effect EL was suggested by Carreras *et al.*<sup>41</sup> The authors developed a multitunnel-junction model to simulate charge transport in nc-Si MOS field-effect transistor structures and field-effect EL using a simple rate equation. Showing good agreement with their model, the authors stated that impact excitation of the nanocrystals by electrons and holes injected from the same silicon substrate is the origin of the field-effect EL. A large difference in the tunneling times of electrons and holes is the main argument of their work. The tunneling times were calculated within the Wentzel–Kramers–Brillouin approximation. However, tunneling time

dependence on bias voltage has a more complex serrated shape,<sup>25</sup> and so this argument should be taken with some precaution.

#### IV. CONCLUSIONS

Few nanometer-thick nc-Si/SiO<sub>2</sub> ML LEDs were grown by PECVD. The operating voltages of our LED are less than 5 V, which is of importance for possible nc-Si LED applications. The turn-on voltage of our LEDs is 1.4–1.7 V, which is less than 3.2 and 4.7 V corresponding to the barrier heights at the silicon oxide interface for electrons and holes, respectively. To the best of our knowledge, this is the lowest turn-on voltage value reported so far for this type of devices. Electrical injection in our LED is controlled by direct charge tunneling between silicon nanocrystals in contrast to Fowler–Nordheim tunneling that controls the injection in the LED operating at high voltages. The EL emission peaks in the visible to near-infrared region in accordance with the nanocrystal sizes.

Time-resolved EL experiments were performed by driving the LED with a square waveform voltage. Under such a pulsed excitation, an enhanced EL emission is observed at the gate bias transitions, which decays in the time scale of a few tens of microseconds. The EL emission is enhanced by a factor of 4 at the driving frequency of 50 kHz. This could be of interest for the applications in which LED is driven with an ac.

The device power efficiency is larger than the power efficiency of a corresponding single layer LED with the value of 0.01% at the direct current of 1 μA. This is believed to be due to the better quality of the barrier oxide, to smaller tunneling barriers, and to the controlled nc-Si formation. The device efficiency could be further improved by achieving a better control over the PECVD growth of nanometer-thick layers and hence better quality of nanocrystals and silicon oxide.

#### ACKNOWLEDGMENTS

We acknowledge support of Intel Corporation and of EC through the project ICT-FP7-224312 HELIOS.

<sup>1</sup>S. Ossicini, L. Pavesi, and F. Priolo, *Light Emitting Silicon for Micro-Photonics* (Springer, Berlin, 2003).

<sup>2</sup>A. T. Fiory and N. M. Ravindra, *J. Electron. Mater.* **32**, 1043 (2003).

<sup>3</sup>*Device Applications of Silicon Nanocrystals and Nanostructures*, edited by N. Koshida (Springer, New York, 2009).

<sup>4</sup>J. Maserjian, *J. Vac. Sci. Technol.* **11**, 996 (1974).

<sup>5</sup>G. F. Grom, D. J. Lockwood, J. P. McCaffrey, H. J. Labbé, P. M. Fauchet, B. White, Jr., J. Diener, D. Kovalev, F. Koch, and L. Tsybeskov, *Nature (London)* **407**, 358 (2000).

<sup>6</sup>P. Photopoulos, A. G. Nassiopoulou, D. N. Kouvatso, and A. Travlos, *Mater. Sci. Eng., B* **69–70**, 345 (2000).

<sup>7</sup>V. Vinciguerra, G. Franzo, F. Priolo, F. Iacona, and C. Spinella, *J. Appl. Phys.* **87**, 8165 (2000).

<sup>8</sup>M. Zacharias, J. Heitmann, R. Scholz, U. Kahler, M. Schmidt, and J. Bläsing, *Appl. Phys. Lett.* **80**, 661 (2002).

<sup>9</sup>L. Zhang, K. Chen, L. Wang, W. Li, J. Xu, X. Huang, and K. Chen, *J. Phys.: Condens. Matter* **14**, 10083 (2002).

<sup>10</sup>G. Franzo, M. Miritello, S. Boninelli, R. Lo Savio, M. G. Grimaldi, F. Priolo, F. Iacona, G. Nicotra, C. Spinella, and S. Coffa, *J. Appl. Phys.* **104**, 094306 (2008).

<sup>11</sup>Z. H. Lu, D. J. Lockwood, and J.-M. Baribeau, *Nature (London)* **378**, 258 (1995).

- <sup>12</sup>L. Tsybeskov, K. D. Hirschman, S. P. Duttagupta, M. Zacharias, P. M. Fauchet, J. P. McCaffrey, and D. J. Lockwood, *Appl. Phys. Lett.* **72**, 43 (1998).
- <sup>13</sup>Z. Gaburro, G. Pucker, P. Bellutti, and L. Pavesi, *Solid State Commun.* **114**, 33 (2000).
- <sup>14</sup>R. Rölver, S. Brünninghoff, M. Först, B. Spangenberg, and H. Kurz, *J. Vac. Sci. Technol. B* **23**, 3214 (2005).
- <sup>15</sup>O. Jambois, H. Rinnert, X. Devaux, and M. Vergnat, *J. Appl. Phys.* **98**, 046105 (2005).
- <sup>16</sup>M. Wang, A. Anopchenko, A. Marconi, E. Moser, S. Prezioso, L. Pavesi, G. Pucker, P. Bellutti, and L. Vanzetti, *Physica E (Amsterdam)* **41**, 912 (2009).
- <sup>17</sup>S. Prezioso, A. Anopchenko, Z. Gaburro, L. Pavesi, G. Pucker, L. Vanzetti, and P. Bellutti, *J. Appl. Phys.* **104**, 063103 (2008).
- <sup>18</sup>S. M. Hossain, A. Anopchenko, S. Prezioso, L. Ferraioli, L. Pavesi, G. Pucker, P. Bellutti, S. Binetti, and M. Acciarri, *J. Appl. Phys.* **104**, 074917 (2008).
- <sup>19</sup>D. J. DiMaria, J. R. Kirtley, E. J. Pakulis, D. W. Dong, T. S. Kuan, F. L. Pesavento, T. N. Theis, J. A. Cutro, and S. D. Brorson, *J. Appl. Phys.* **56**, 401 (1984).
- <sup>20</sup>B. De Salvo, G. Ghibaudo, P. Luthereau, T. Baron, B. Guillaumot, and G. Reimbold, *Solid-State Electron.* **45**, 1513 (2001).
- <sup>21</sup>J. Cai and C.-T. Sah, *J. Appl. Phys.* **89**, 2272 (2001).
- <sup>22</sup>G. Franzò, A. Irrera, E. C. Moreira, M. Miritello, F. Iacona, D. Sanfilippo, G. Di Stefano, P. G. Fallica, and F. Priolo, *Appl. Phys. A: Mater. Sci. Process.* **74**, 1 (2002).
- <sup>23</sup>S.-H. Lo, D. A. Buchanan, and Y. Taur, *IBM J. Res. Dev.* **43**, 327 (1999).
- <sup>24</sup>A. Schenk and G. Heiser, *J. Appl. Phys.* **81**, 7900 (1997).
- <sup>25</sup>B. Leriche, Y. Leroy, and A. S. Cordan, *J. Appl. Phys.* **100**, 074316 (2006).
- <sup>26</sup>J. De La Torre, A. Souifi, A. Poncet, C. Busseret, M. Lemiti, G. Bremond, G. Guillot, O. Gonzalez, B. Garrido, J. R. Morante, and C. Bonafos, *Physica E (Amsterdam)* **16**, 326 (2003).
- <sup>27</sup>A. Marconi, A. Anopchenko, M. Wang, G. Pucker, P. Bellutti, and L. Pavesi, *Appl. Phys. Lett.* **94**, 221110 (2009).
- <sup>28</sup>K. Seino, F. Bechstedt, and P. Kroll, *Nanotechnology* **20**, 135702 (2009).
- <sup>29</sup>J. Heitmann, F. Muller, L. Yi, M. Zacharias, D. Kovalev, and F. Eichhorn, *Phys. Rev. B* **69**, 195309 (2004).
- <sup>30</sup>Y. Liu, T. P. Chen, L. Ding, M. Yang, J. I. Wong, C. Y. Ng, S. F. Yu, Z. X. Li, C. Yuen, F. R. Zhu, M. C. Tan, and S. Fung, *J. Appl. Phys.* **101**, 104306 (2007).
- <sup>31</sup>O. L. Lazarenkova and A. N. Pikhtin, *Semiconductors* **32**, 992 (1998).
- <sup>32</sup>V. Ioannou-Sougleridis, B. Kamenev, D. N. Kouvatso, and A. G. Nassiopoulou, *Mater. Sci. Eng., B* **101**, 324 (2003).
- <sup>33</sup>M. Kulacki, U. Serincan, R. Turan, and T. G. Finstad, *Nanotechnology* **19**, 455403 (2008).
- <sup>34</sup>K. I. Mazzitello, H. O. Martin, and H. E. Roman, *Eur. Phys. J. B* **54**, 315 (2006).
- <sup>35</sup>R. J. Walters, G. I. Bourianoff, and H. A. Atwater, *Nature Mater.* **4**, 143 (2005).
- <sup>36</sup>V. Filip, H. Wong, C. K. Wong, and D. Nicolaescu, *J. Vac. Sci. Technol. B* **26**, 813 (2008).
- <sup>37</sup>R. J. Walters, "Silicon nanocrystals for silicon photonics," Ph.D. thesis, California Institute of Technology, 2007.
- <sup>38</sup>Th. Dittrich, V. Yu. Timoshenko, J. Rappich, and L. Tsybeskov, *J. Appl. Phys.* **90**, 2310 (2001).
- <sup>39</sup>A. M. Emel'yanov, Yu. A. Nikolaev, N. A. Sobolev, and T. M. Mel'nikova, *Semiconductors* **38**, 610 (2004).
- <sup>40</sup>A. Irrera, D. Pacifici, M. Miritello, G. Franzò, F. Priolo, F. Iacona, D. Sanfilippo, G. Di Stefano, and P. G. Fallica, *Appl. Phys. Lett.* **81**, 1866 (2002).
- <sup>41</sup>J. Carreras, O. Jambois, S. Lombardo, and B. Garrido, *Nanotechnology* **20**, 155201 (2009).
- <sup>42</sup>O. Jambois, J. Carreras, A. Pérez-Rodríguez, B. Garrido, C. Bonafos, S. Schamm, and G. Ben Assayag, *Appl. Phys. Lett.* **91**, 211105 (2007).